Icarus 316 (2018) 191–204

Contents lists available at ScienceDirect

Icarus

journal homepage: www.elsevier.com/locate/icarus

Dawn mission's search for satellites of Ceres: Intact protoplanets don't have satellites

Lucy A. McFadden[a,*], David R. Skillman[a], N. Memarsadeghi[a], U. Carsenty[b], S.E. Schröder[b], J.-Y. Li[c], S. Mottola[b], Max Mutchler[d], Brian McLean[d], S.P. Joy[e], C.A. Polanskey[f], M.D. Rayman[f], P.D. Fieseler[f], M.V. Sykes[c], A. Nathues[g], P. Gutiérrez-Marques[g], H.U. Keller[b,h], C.A. Raymond[f], C.T. Russell[e]

[a] NASA Goddard Space Flight Center, Greenbelt, MD 20771, USA
[b] DLR - German Aerospace Center, Institute of Planetary Research, Berlin, Germany
[c] Planetary Science Institute, Tucson, AZ 85719, USA
[d] Space Telescope Science Institute, Baltimore, MD 21210, USA
[e] Institute of Geophysics and Planetary Physics, University of California, Los Angeles 90095, USA
[f] Jet Propulsion Laboratory, California Institute of Technology, Pasadena, CA 91109, USA
[g] Max-Planck Institute for Solar System Research, Göttingen 37077, Germany
[h] Institut für Geophysik und extraterrestrische Physik (IGEP), Universität Braunschweig, Mendelssohnstr. 3, 38106 Braunschweig, Germany

ARTICLE INFO

Article history:
Received 28 November 2016
Revised 7 February 2018
Accepted 13 February 2018
Available online 16 February 2018

Keywords:
Dwarf planet Ceres
Asteroids
Satellites of asteroids
Asteroid Ceres

ABSTRACT

Upon its approach to orbit the dwarf planet Ceres in early 2015, optical navigation and dedicated satellite search images were acquired with the Dawn mission's framing camera 2. A team of searchers individually processed and examined the images for evidence of objects moving with Ceres. Completeness of search with respect to the space searched was calculated as a function of distance to Ceres and found to be complete down to 15 Ceres radii (Ceres' mean radius is 470 km). Upper limits of detectable magnitude were determined for each observed set of images and an upper limit in size was calculated assuming for the putative objects, Ceres' geometric albedo of 0.11. Nothing was found associated with Ceres down to a radius of 12 m for the most sensitive search, and down to a radius of 323 m for the least sensitive search circumstances. Examination of the physical properties of the 41 largest and most massive main belt asteroids suggests that large asteroids without satellites are intact and their interiors have internal strength. This is consistent with results from the Dawn mission at both Vesta and Ceres. Ceres' volatile-rich composition also is a likely contributor to both the absence of satellites at Ceres and of Ceres meteorites at Earth. These results suggest that collisional disruption creating rubble pile structure is a necessary condition for formation of satellites around main belt asteroids.

Published by Elsevier Inc.

1. Introduction

Scientists have searched for satellites around asteroids since their first discovery in the early 19th century to inventory the content and structure of the Main Asteroid Belt (e.g. Merline et al., 2002) and the Trans-Neptune region of the Solar System (Noll et al., 2008). Sometimes we find satellites (e.g. Chapman et al., 1995; Merline et al., 1999; Merline et al., 2002; Margot et al., 2002; Ryan et al., 2004; Marchis et al., 2005, 2016, 2008, 2009; Margot et al., 2015; Johnston, 2015; Marsset et al., 2016), and many times, upper limits to the sizes of satellites that are *not* found are reported (Gehrels et al., 1987; Veverka et al., 1999; Merline et al., 2001; Marchis et al., 2016; Busch et al., 2009; Bieryla et al., 2011; McFadden et al., 2015; DeMario et al., 2016). The presence or absence of satellites of asteroids provide observational clues to the formation and evolution of the asteroid belt and contribute to our understanding of the structure of the Solar System.

Searches for natural satellites of the largest main belt asteroids have been carried out with available observational techniques (Gehrels et al., 1987; Marchis et al., 2016; Walsh, 2009) including light curve analysis, adaptive optics, radar and direct imaging. In situ spacecraft provide an opportunity to search at closer range and imaging from the Galileo spacecraft revealed a satellite orbiting the asteroid Ida (Chapman et al., 1995). Prior to NASA's Dawn

* Corresponding author at: Planetary Systems Laboratory, Code 693, Goddard Space Flight Center, 8800 Greenbelt Rd, Greenbelt, MD 20771, USA.
E-mail addresses: lucy.mcfadden@nasa.gov, lucy.mcfadden@verizon.net (L.A. McFadden).

https://doi.org/10.1016/j.icarus.2018.02.017
0019-1035/Published by Elsevier Inc.

spacecraft orbiting both Ceres and Vesta, the two largest bodies in the Main Belt (mean radius 470 and 262 km respectively), existing ground and space-based telescopes were deployed to search for any possible moons orbiting them (McFadden et al., 2012, 2015; Li et al., 2010; Bieryla et al., 2011; De Mario et al., 2016). The limiting magnitude of the search, and a resultant size, assuming a satellite with the same albedo as Ceres and Vesta, were determined. For Ceres, the possible detectable size was 1–2 km diameter (Bieryla et al., 2011). Li et al. (2010) used a coronograph and imaged around Ceres with the Keck telescope and determined a size limit of 1 km at 3 Cerean radii. Most recently, DeMario et al. (2016) determined a diameter of 925 m upper limit out to 5 Cerean radii and 48 m to a distance of 205,000 km (433 Ceres radii) using images from Hubble Space Telescope's Wide Field Camera 3.

Here we report the results of the search conducted using one of the framing cameras (Sierks et al., 2011) on the Dawn spacecraft as it approached Ceres (e.g. Rayman, 2017). We include our image acquisition plan, results of multiple approaches by coauthors searching for satellites and an analysis of the detectable upper limit to the size of a satellite if any exists. We conclude that there are no natural satellites or moons of Ceres down to a radius of 12–323 m assuming Ceres' albedo, consistent with and smaller than the results of DeMario et al. (2016).

We then examine the published physical properties (mass, density, spin rate) of the 41 largest and most massive main belt asteroids to consider the conditions that preclude or favor satellite formation and discuss previously published mechanisms of multiple system formation. We hypothesize that large and massive asteroids without satellites most likely have strong interiors and have not been completely disrupted by catastrophic collisions and because of this, they do not have satellites.

2. Imaging strategies and observations

Our satellite search imaging strategy was designed considering both previous experience from the Dawn mission's search for satellites at Vesta (McFadden et al., 2015) and the state of the spacecraft on approach to Ceres with only two of four reaction wheels still operational (Rayman and Mase, 2014). We followed principles of the redesigned science plan for Ceres (Polanskey et al., 2014, 2016) carrying out a science-driven satellite search. From the search at Vesta we found that 20 s (short) exposures were more efficient than the 270 s (long) exposures targeting fainter satellites because many more images could be searched with little loss in sensitivity. To place this in context, consider that a moving object sets its own exposure time by remaining on a given 94 μrad pixel for a time much shorter than the full duration of an exposure. As a consequence, the signal-to-noise per pixel of the source would not increase with increasing exposure time, thereby not contributing to improving the detection limit. This effect is generally referred to as trail loss. In our previous analysis of simulated moving targets implanted in images, the 270 s exposures at Vesta were 13.5 times longer than the short exposures but yielded only 1.1 times the number of objects found in the shorter exposures (McFadden et al., 2015). All dedicated satellite search exposures at Ceres were 2 s long and performed in the clear filter, an exposure established taking into account the spacecraft's larger attitude errors resulting from the compromised attitude control. The drift, measured as the spacecraft coasted from one edge of a deadband to another, was ~1 px/s, on average, with some excursions higher. The deadband width is different in each of the control axes so the camera boresight traced out a broken linear path (Fig. 1). We set the exposure time by considering that the nominal drift rate of 90 μrad/s, almost exactly 1 px/s, would produce acceptable stellar images with minimal smear. Stellar images can fall on the boundary of two pixels or the corner of four pixels so it was concluded that a smear of one extra pixel would be acceptable – this set the exposure time to 2 s. Power spectrum simulations by the attitude control team showed that the drift velocities would largely remain below 1 px/s. Satellite search images were acquired and searched during optical navigation (OpNav) sessions, and called ride-along images. We also searched for satellites using the rotational characterization (RC) sequences RC1, RC2 and parts of RC3 that are described below in the order in which they were acquired.

Fig. 1. Sum of 40 OpNav1 images (Nathues et al., 2016a), with no registration, shows the spacecraft's drift over 61 minutes. Exposure times alternated between 0.048 and 1 s. Perfect pointing would lead to a single disk.

2.1. Optical navigation ride along imaging

On approach to Ceres, the Dawn spacecraft completed seven optical navigation imaging sessions pointing at Ceres using framing camera 2 (FC2) (Nathues et al., 2016a,b,d,f,g,h,i). The first two (Nathues et al., 2016a,b) consisted of 40 clear-filter images of alternating 48 and 1000 ms exposures (Figs. 1 and 2). OpNav 3–7 (Nathues et al., 2016d,f,g,h,i) included 180 additional satellite search ride-along images of 2 s exposures with Ceres nearly centered in the field of view (FOV). Up to five different searchers processed and searched the images for evidence of objects other than stars and Ceres. Table 1 contains observing dates, positions and parameters needed to calculate an upper limit of detection of a possible satellite and its size that is presented in Section 4.

2.2. Dedicated satellite search

Two additional dedicated satellite search segments were planned and executed on either side of OpNav 3, named MoonSearch 1A, 1B (Nathues et al., 2016c,e). Commanded pointing was offset from Ceres (Fig. 3, top and bottom). Search 1 included 12 imaging activities with each activity consisting of sixteen 2 s exposures using the clear filter with 9 s cadence between exposures (Fig. 3, middle). The latter was set by the fastest image repetition rate recommended for FC operations. There was then a ~100 s wait between each activity (Fig. 3, middle). After a set of 4 activities, called a 'station', observations were paused for ~45 min and the set of 4 activities were conducted twelve times. There was a pause of 3.75 h between satellite search 1 and 2. For the second search, the framing camera pointed as depicted in Fig. 3, bottom and consisted of 16 instances of the same activity (not shown in Fig. 3).

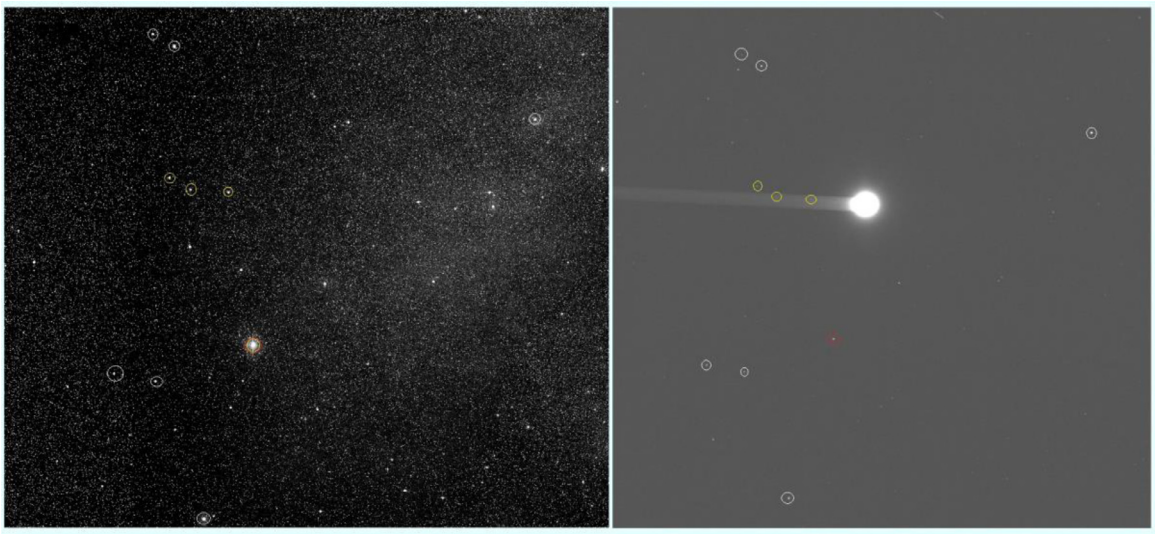

Fig. 2. Framing camera's orientation in space. Left: a 5° × 5° sky survey photograph centered on image 32,651, the first OpNav 1 frame. Right: framing camera image 32,651 showing Ceres (brightest feature), the CCD's readout smear (a broad trail extending from Ceres). Bright stars used to compute the image orientation with respect to the equatorial coordinate system are circled in both Left and Right.

Table 1
Observing Parameters for Ceres Satellite Search including estimated detection limits in Magnitude and upper limits in Radius of Possible Satellites.

UTC	Sequence	Range(km)	Phase (°)	Sub-Ceres Dec (°)	Sun-SC (AU)	ExpTime (s)	V-Mag	Mag(PhaseCorr)	Radius (m)	Searcher
2015-01-13T20:20:50	OPNAV 1	383,111	26	-22	2.83	1	10.8	9.4	191	1,2,3,4,5
2015-01-25T22:21:22	OPNAV 2	238,100	23	-19	2.84	1	10.8	9.5	113	1,2,3,4,5
2015-02-04T05:01:06	MoonSearch 1A	147,707	19	-15	2.85	2	11.7	10.5	44	1
2015-02-04T07:46:06	OPNAV 3	146,722	18	-15	2.85	2	12.8	11.7	26	1,3,4,5
2015-02-04T11:03:06	MoonSearch 1B	145,548	18	-15	2.85	2	11.7*	10.6	42	1,3
2015-02-04T11:03:06	MoonSearch 1B'	145,548	18	-15	2.85	2	12.8*	11.7	25	1
2015-02-25T19:07:36	OPNAV 4	40,450	96	32	2.86	2	12.8	9.0	25	1,2
2015-03-02T00:32:56	OPNAV 5	49,417	123	30	2.86	2	12.8	7.5	59	1,2
2015-04-10T08:06:46	OPNAV 6	33,734	131	45	2.89	2	12.8	6.9	55	1,2
2015-04-15T08:11:03	OPNAV 7	22,827	90	85	2.89	2	12.8	9.2	12	1,2
2015-04-29T06:20:01	RC3 HIGH PHASE NORTH 1A	14,002	155	20	2.90	5	10.5	1.1	323	1

Notes: UTC is time of first image in each Sequence (Nathues et al., 2016a,b,c,d,e,f,g,h,i,j). *MoonSearch 1B limiting magnitude calculated from 16 stacked images, effective exposure time of 32 s. MoonSearch 1B' is limiting magnitude calculated from 64 stacked images, effective exposure time of 128 s.

The 100 s wait time was to allow any orbiting body to change its position relative to Ceres. There was a trade-off in that a shorter wait time might not allow much satellite motion but a longer wait time would risk allowing attitude drift of the spacecraft to reduce the amount of image overlap needed for blinking (searching).

The two offset pointings were chosen to include Ceres' equatorial plane. If there were any satellites physically located between the spacecraft and Ceres, we would have a fainter detection limit, because they are closer, and there would be a chance to observe them twice if they were in prograde equatorial orbits, the most likely case. In this case any satellite in the first search region could possibly move into the second search region, improving the reliability of the detection and offering improved chances of a higher quality orbit determination.

2.3. Star tracker search

The Dawn spacecraft carries two Sodern SED-16 star-trackers (Krebs et al., 2000) to provide attitude knowledge. Of these, the +Y axis tracker (Vanelli et al., 2008) was used to search for satellites of Ceres from Jan 27, 2015 to Feb. 21, 2015, as the spacecraft traveled from 218,000 km to 41,000 km range from Ceres. The star tracker consists of a 1024 by 1024 pixel CCD masked to a circular field of view of 12.5° half-angle. The optical system's response is close to the R curve in the UVBRI photometric system (Bessell, 1990) and could detect a neutrally-colored, C-type satellite with a Ceres-like albedo as above, down to visual magnitude +4.0 with 20 ms integration. A very red body might be detected down to magnitude +5.5 or better. Under ideal illumination conditions and absent opposition surge, the star tracker could detect a 0.5 km radius C-type object at a distance of 60,000 km. A calibration using non-variable stars found the 1-sigma deviation in the magnitude measurements to be 0.035 magnitude and the 1-sigma error in position measurements to be 17″. The instrument carries no optical filters.

Data for the satellite search were sampled by placing the star tracker into a mode reporting the measured position and magnitude of up to 17 objects. These objects can be stars, noise due to energetic particles or distant astronomical bodies including, potentially, satellites of Ceres. Data were collected in "sessions" consisting of ten samples taken over 2 s to provide multiple measurements in order to allow subtraction of the noise which varies from sample to sample. Each of these sessions was then repeated at 2 h intervals to capture the motion of any satellites across the field of view. Data were collected when the spacecraft was using its ion engine for maneuvering into orbit. This was to avoid competing for data volume with the science instruments, which are normally off while the ion engine is in use. Since directed propulsion requires specific spacecraft orientations and the star tracker is fixed to the spacecraft body, the star tracker pointing was not targeted but rather rode along observing whatever section of the sky was presented to it (opportunistic pointing).

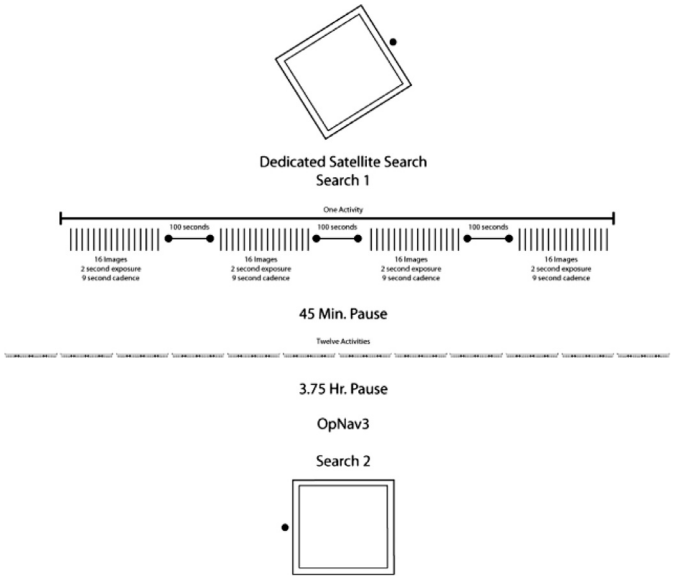

Fig. 3. Dedicated satellite search 1A beginning February 4, 2017. Top: Framing camera footprint with respect to Ceres (solid dot) for Search 1A pointing. Inside box is $5° \times 5°$, outside box extends the fov by 0.64° due to spacecraft drift. Middle: Schematic of data acquisition where vertical line is one image acquisition. Four activities comprise one station and acquisition sequence was conducted 12 times for satellite search 1A. Satellite search 1B used the same pattern, conducted 16 times. Bottom: orientation of image frame with respect to Ceres (solid dot) for search 1B.

After February 21, 2015, an anomaly occurred in star tracker 1. Though it was quickly corrected, Dawn project and science personnel determined the risk to the mission exceeded the potential for further scientific gain and the star tracker mode of satellite search was terminated. While several investigations of candidate satellites in the data set were initiated, none of these candidates met or exceeded the minimum criteria for detection of a satellite.

2.4. Final satellite search during rotational characterization 3 (RC3)

RC3 was Dawn's first science orbit at Ceres, at an average altitude of 13,600 km. Although no satellite searches had been planned during this phase, we realized that high phase dust/plume search images would be comparable to earlier satellite search imaging. Upon closer examination, only the High Phase North001 images had overlapping frames suitable for satellite searching. These had a cadence of three minutes. Images acquired during this phase were searched and the results are reported below in Section 3.1.

3. Data processing and search approaches

Five individual searchers calibrated, registered, stacked and searched images for evidence of moving objects. Searchers 1 and 2 determined the limiting magnitude of their efforts through calibration with star catalogues accessed by the software used. In McFadden et al. (2015), we calibrated the searchers' magnitude detection limits using implanted moving objects. Given the time and effort involved in searching we saw no reason to repeat that exercise for this effort. All searchers employed image processing techniques to enhance detection of motion of objects relative to Ceres. Searcher 5 used an algorithm derived for computer-automated object detection that compares identified objects to those in a star catalogue (McFadden et al., 2015 and references therein). Multiple people searched the data with the idea that different approaches and more eyes would improve the rigor of our efforts. These efforts were also limited by available personnel and resources. No satellites were found by any searcher. We report the approaches and what *was* observed below and in Section 4. In-flight calibration of Dawn's framing cameras can be found in Schröder et al. (2013). Every observer performed image registration that isolates image features that can be either an object in Ceres' orbit, particles detached from the spacecraft, hot or cold pixels or cosmic rays. To meet the criterion of a Ceres moon, any suspected satellite has to be present in each image and to have an image point spread function. None were found.

3.1. Searcher 1

The images were processed via the astrometry.net service (Lang et al., 2010) using the USNO-B1.0 catalogue (http://ad.usno.navy.mil/star/star_cats_rec.html) to produce world coordinate system (WCS) information for each image. USNO-B1.0 presents right ascension and declination, proper motion and magnitude estimates. It is estimated that the positional error at current epoch is near 200 mas (milliarcseconds). Registering the stars permits co-adding of images and thus establishes a reference frame for detecting motion while blinking. Co-adding furthermore, increases the sensitivity to faint objects such as slow-moving satellites or fixed stars. Ceres and the background stars are in a slightly different position on each frame due to attitude drift. Because of spacecraft motion perpendicular to the bore sight of FC2, Ceres moves relative to the background stars (parallax motion). Working with raw images with no hot-pixel subtraction adds a difficulty in that by registering to the stars, all the hot pixels are in apparent motion. Because in this late phase of the mission there are many hot pixels, their motion is easily noted by their common direction and rate. It is only the objects that move differently than the hot pixels that catch our interest. Blinking co-added sets of images allows us to search for those objects that have regular motion relative to the fixed stars. If we had found any potential satellite candidates, their positions would have been reported using the UCAC3 positions which have an accuracy far better than the centroid accuracy of the FC point spread function.

Images were stacked in sets of 16 to produce 4, 32 s exposures. These four images were blinked in the program Astrometrica (Raab, 2013) that uses the UCAC3 star catalog (http://tdc-www.harvard.edu/catalogs/ucac3.html). Blinking consists of displaying each of the frames for a short interval, then the next frame, and then repeated continuously. The blinking was repeated, with the searcher visually inspecting sections of the image stacks methodically looking for moving objects with regular motion. Some artifacts appeared to be moving, but none had a stellar point spread function representing light passing through the optics. If the attitude drift velocities happened to be slow, several stations could then be blinked together, co-adding the 64 images of each station to produce three frames each of effective exposure time of 128 s. These are displayed in Fig. 4.

3.1.1. Satellite searches during RC3

During RC3 (Fig. 5), it was possible to have good overlap for up to ten 5 s images and the presence of the dark surface of Ceres allowed inspection of the nadir field for moving objects that might cross below Dawn. Ceres occupied a large part of the central FC FOV during RC3 imaging and the standard astrometric registration failed because of missing stars. We were able to isolate corners of $\sim 2° \times 2°$ FOV that could be astrometrically solved and thus provide an inferred solution for each field. The prime value of an astrometric solution is both registration and prediction of background asteroids that could confuse the search. Because there are very few (probably zero) background asteroids it was decided to bypass the normal astrometric registration and employ a manual process.

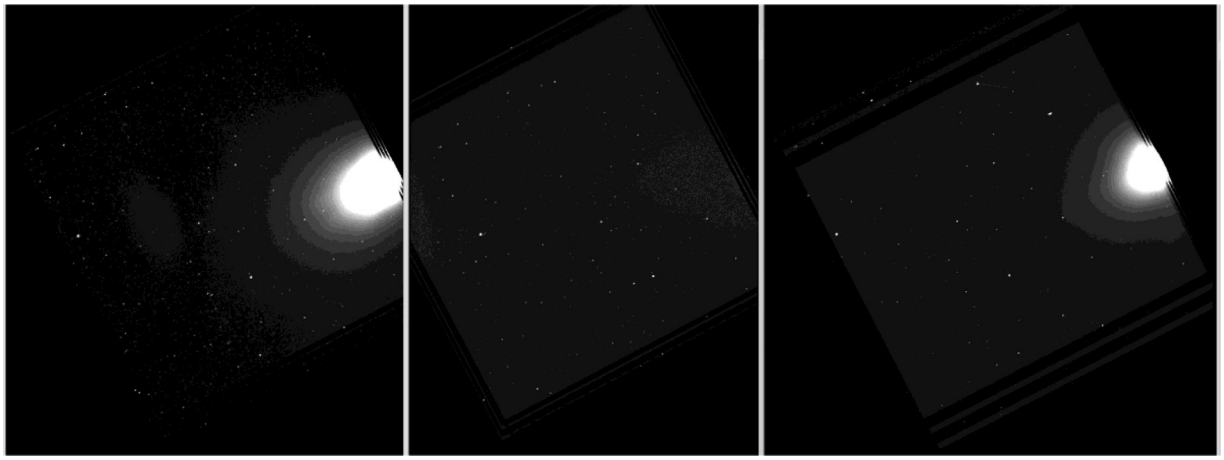

Fig. 4. Three, full-frame (5.5° × 5.5°), co-registered stacks of 64 images from moon search 1. These three sets were blinked to affect the most sensitive search to detection limit of magnitude 12.8. The first image in the left stack is FC21A0032731_15035050107F1B.fit.

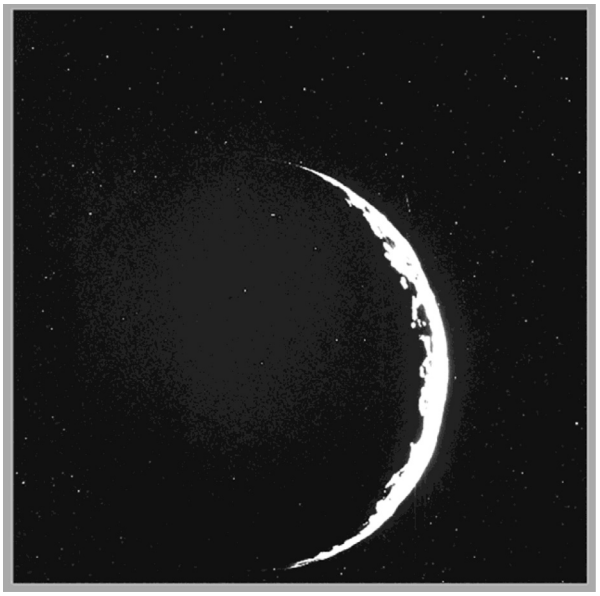

Fig. 5. RC3 North image (FC21A0035500_15119072617F1A) displayed so as to reveal background stars used to register, blink and search for satellites.

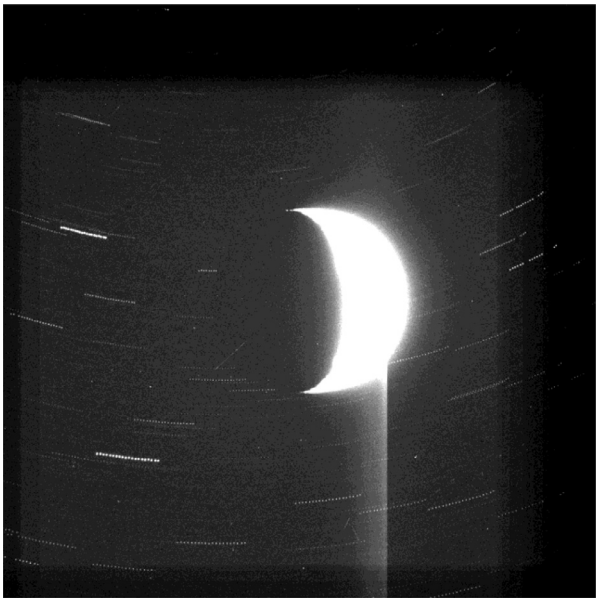

Fig. 6. OpNav 6 co-added images with outside frame 500 × 500 pixels from Ceres center.

The High Phase North001 data were broken up into 18 sets of ten, 5 s images. For each set the individual images were inspected first for pairs of alignment stars that were well-separated, and remained both on-frame and unblocked by Ceres for all ten images. Such pairs were found for 16 of the 18 sets. The other two sets were shortened to 9 or 8 frames for which there were acceptable alignment stars. Each set covered 30 min for a total of 9 h of imaging.

Each set was then automatically registered to these alignment stars to produce ten images in which the background stars were at the same fixed positions. Maxim-DL-IP (2008), a software program that is designed to control any commercial CCD camera, control any commercial telescope, and provide the ability to calibrate and reduce any CCD image was used to perform this alignment. The image processing (-IP) version does not incorporate camera and telescope control functions, thus freeing up memory space for intensive image manipulation. It does not use a star catalog and was used only for blinking in complex situations that Astrometrica could not handle. The ten images were then expanded by a factor of four and the blinked images were searched for moving objects. Any moving objects brighter than magnitude 10.5 would have been detected.

3.2. Searcher 2

A series of 5 images from OpNav 1 were co-added and searched visually for trails of objects moving in a direction different than background stars. For OpNav 2 images, all 1 s exposures on Ceres were registered, expanded by a factor of 2 and an 800 × 800 pixel sub-frame was extracted from the original image. The first 3 and last 3 images were added, then the first from last was subtracted, as was also done in McFadden et al. (2015). OpNav 4 motion was moderate and almost in one direction therefore all 20, 2 s exposure images were registered, adding the first 10 and second 10. The background stars form a series of dotted lines. For OpNav 5 and 6 two techniques were used. Ride-along search images were co-added in stacks of 20, followed by looking for evidence of trails moving in directions different from background stars (Fig. 6). Secondly, the stacks were blinked and searched close to Ceres. The limiting magnitude is ~11.5.

Twenty, 1.5 s images were registered on Ceres and co-added in OpNav 6 (Fig. 6). The first image is FC21A0034269, and subsequent images are named by adding 11 to the name of the first. Satellites would have a point spread function and a trail in a direction different from the background stars. The streak at the 8 o'clock position is a cosmic ray because it has no point spread function and is partly illuminated on the dark side of Ceres. Three additional cosmic rays can be seen in this image too.

3.3. Searcher 3

The dedicated satellite search method of searcher 3 is illustrated in Fig. 7. We began by averaging all images in the sequence acquired at each observational station of the satellite search activity. To increase the probability of detection we inspected the average displayed on a logarithmic brightness scale (Fig. 7a). By means of their proper motion moons would show up as trails similar to stars, but with different direction and length. As a sanity check, we also combined the first, middle, and last image acquired at the station in a Red-Green-Blue color composite (Fig. 7b). Real objects like stars and moons, i.e. not cosmic rays, must show up in all three colors on a trail. This revealed no obvious moon candidates. We then registered all images within a sequence to the middle image of the sequence. In the average of the registered images (again displayed on a logarithmic brightness scale), hot and cold pixels show up as thin trails (Fig. 7c). Moons with large enough proper motion would show up as a faint trail that is wider than that of hot pixels due to the PSF. Note that the edges of the frame do not have complete overlap and cannot be searched. To assess the nature of a typical hot pixel trail a fake hot pixel was inserted in the center of all images prior to averaging. Due to the unavailability of recent dark frames hot pixels were plentiful, but no obvious moon candidates were identified. The searcher then subtracted the median of the registered images (Fig. 7d) from the average of the registered images. This method removes the celestial background and leaves only cosmic rays, moons, and hot pixel trails (Fig. 7e). Alternatively, we applied a 3-pixel wide median filter to each registered image row prior to calculating the median over all images (Fig. 7f). This ensures the removal of hot pixel trails, but may also decrease the brightness of moon trails. No moving objects associated with Ceres were found and the photometric limit of detection was not determined by this searcher.

3.4. Searchers 4 and 5

Searcher 4 uses unsharp-mask filtering to enhance high frequency signal and decrease obscuration from scattered light. A visual search for evidence of a point spread function is made. After registration, the frames were blinked looking for point-spread functions moving with Ceres. This searcher searched OpNav's 1–3 including the dedicated satellite search sequences. No moving objects associated with Ceres were detected.

Searcher 5 searched OpNav's 1–3 using an algorithm for automated object detection and compares identified objects to those in star catalogues. Each image was then processed through a series of common pipeline steps including dark removal, bias subtraction, flat-field removal, and unsharp-masking. Following these steps, an image detection algorithm based on DAOPHOT (Stetson, 1987) was applied to find objects with a Gaussian PSF and reject any objects found within a couple pixels of known hot/bad pixels. The approximate WCS solution (Section 3.1) was used to automatically identify stars from the Guide Star Catalog (GSC) (Lasker et al., 2008) and UCAC3 (Zacharias et al., 2010) catalogs. No moving objects associated with Ceres were detected. Limiting magnitudes were determined by performing PSF photometry on all detected objects and then calibrating the relationship using the known magnitudes of stars in the field present in the GSC catalog.

Limiting detection magnitude for OpNav 1 and 2 of 1 s exposures is mag 9.5. The moon search sequence with 2 s exposures had a limiting detection magnitude of 10.6 and OpNav 3, with 1.5 s exposures had a limiting magnitude of 9.9.

3.5. Star tracker search

The star tracker data were returned in a tabular format rather than as an image, and software was created to graphically display the data. All detected objects were plotted against a star chart and run as a movie to allow human reviewers to search for objects moving across the field of view. Positional data from any potential satellites were extracted and sent to a specially modified version of FindOrb (Dymock, 2007), which would attempt to compute the orbit of the body about Ceres, along with orbit residuals and estimated absolute magnitudes.

The minima criteria for a positive discovery of a satellite was its detection in at least three consecutive sessions and following a path with an orbit that closed on Ceres with residuals less than 1′. The data from a session would be rejected if it was found to match any of the following conditions: (1) its position was within the 0.5″ of the expected location of a star in either the star tracker's own catalog, or (2) against stars in the Catalog of Positions and Proper Motions (Bastian and Roser, 1993) and the General Catalogue of Variable Stars (Samus et al., 2001) screened down to visual magnitude +7.0, or (3) against the de430 ephemerides of the planets (Acton, 1996), or (4) the 300 brightest comets and asteroids as determined from the codes_300ast_20100705 ephemerides (Acton, 1996).

4. Results

This search was carried out with images acquired between January 13 and April 29, 2015 when the spacecraft was 383,000–14,000 km from Ceres' center. No known main belt asteroids were present in the FC2 field of view during that time. No trail with a different direction and length relative to the background stars was found in registered and stacked images during any of the OpNav ride along activities. Likewise, nothing was found during blinking of images acquired during the dedicated satellite search, nor by processing and filtering registered and stacked images acquired during RC3. None of the candidates in the star tracker search met nor exceeded the minimum criteria for detection of a satellite.

4.1. Artifacts

An out of focus particle receding from the spacecraft was detected in OpNav 2 and another during the dedicated satellite search (Fig. 7b). Occasionally a glancing cosmic ray produced a long streak (Fig. 6) as described in McFadden et al. (2015). A third artifact type was detected upon examining limb images of Ceres (Fig. 8) during the low altitude mapping orbit (LAMO). In these two images, sunlight illuminates the high point of a crater rim and the rotation of Ceres produces a trail of illuminated pixels that trace Ceres motion and spacecraft drift against the background stars. The trails have different orientations than stars and meet the criterion for objects following Ceres motion, yet the illuminated region is likely a crater wall appearing over Ceres' limb.

4.2. Search completeness

We ran Monte Carlo simulations to assess the completeness of space searched during our satellite search at Ceres and call this

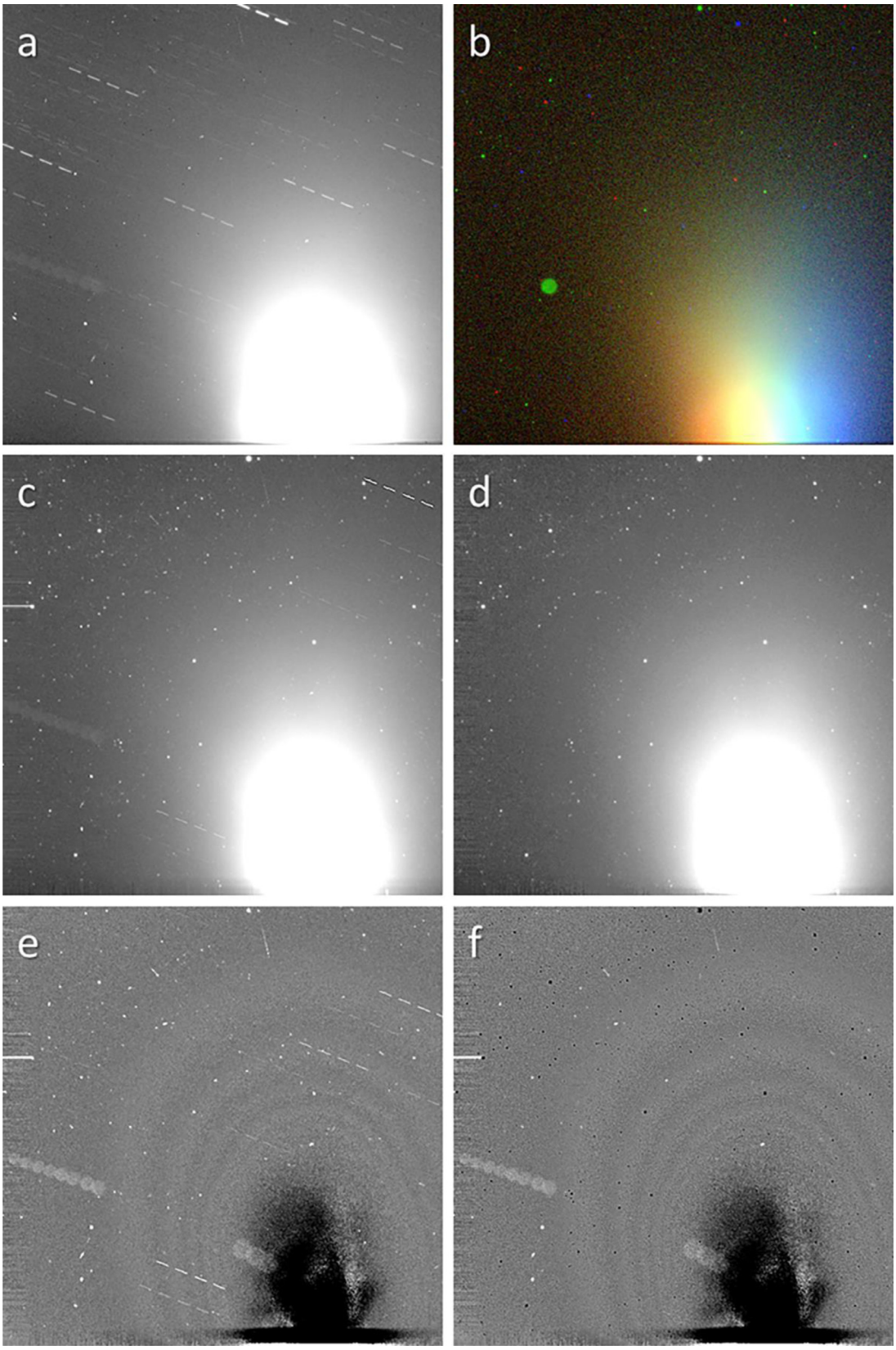

Fig. 7. Satellite search 1 image processing includes a 550 × 550-pixel extraction from lower left image corner. (a) Average of all 64 images (image names ending in 32,731–32,794) acquired in one station as defined in Section 2.2. The bright region at bottom right is stray light from Ceres, which is present just outside the FOV. (b) RBG color composite of the first, middle, and last image of the sequence. An out-of-focus particle observed close to the spacecraft is spherical, larger than star images and visible in green. (c) The average of all images registered to the middle image of the sequence. Note the artificial hot pixel in the upper right corner. (d) The median of all registered images, showing the clean celestial background. (e) The average minus the median ((c)–(d)), revealing the dust particle (overlapping and spherical) hidden in the stray light. (f) As (e) but with the registered images filtered with a 3-pixel wide median filter prior to calculating the median over all images, removing the hot pixel trails. (For interpretation of the references to colour in this figure legend, the reader is referred to the web version of this article) .

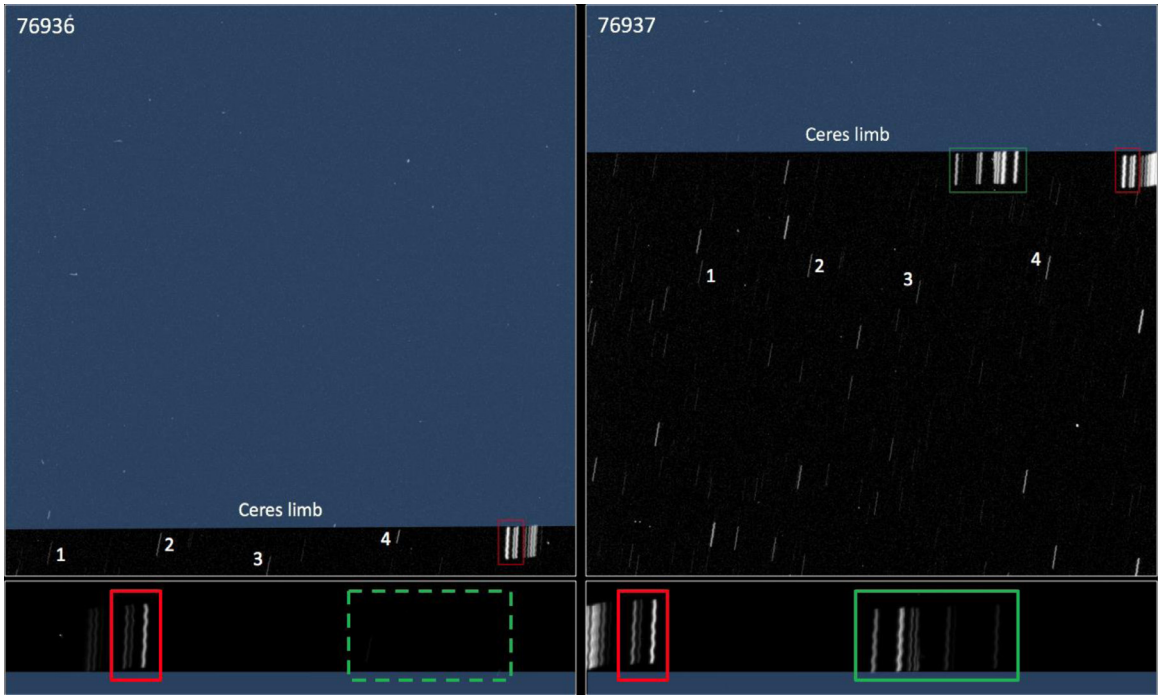

Fig. 8. Two 5 s exposures from LAMO cycle 10 (image 76,936 and 76,937) taken 54.8 s apart are displayed in logarithmic brightness stretch. Two sets of trails are formed by illumination of peaks on a crater wall. Four stars are noted by numbers 1–4 with constant trail brightness and different orientation. Bottom panel: In an expanded view of the limb trails, the group boxed in red (left in each panel) becomes brighter with increased illumination as Ceres rotates. The green group (within dotted rectangle) had not rotated into view in image 76,936 but appeared 54.8 s later (solid box at right). (For interpretation of the references to colour in this figure legend, the reader is referred to the web version of this article.)

"geometric completeness". For this purpose, we generated one million test satellites in circular orbits with orbital radii from 1 to 500 Ceres radii, orbital inclinations uniformly distributed within 10° from the equatorial plane, and their ascending nodes randomly distributed over 0° to 360°. The orbital period of a test satellite is determined by the mass of Ceres and its orbital radius. With uniformly distributed positions in orbits for all test satellites at an arbitrary start time, we calculated their projected coordinates on the sky relative to Ceres at the times that every image was collected. After doing this calculation for all images acquired during the OpNav 3 satellite search phase sequence, if a test satellite appears within the FOVs and is not blocked by Ceres' disk in three or more images, we consider this test satellite as being detected. The completeness of detection at orbital radius r from Ceres' center is then the fraction of satellites with orbital radii between r and $r+dr$ that are detected with respect to all test satellites within this orbital radius range in the simulation. Fig. 9 shows the results of this simulation.

For satellites with orbital radii less than ~15 Ceres radii, our search is complete in a geometric sense, i.e., without considering the scattered light from Ceres that could hide a faint satellite in the glare near Ceres. The arc that a satellite spends in orbit behind Ceres approximately follows $\arcsin(r^{-1}) \sim r^{-1}$ for large r, while its angular orbital speed follows $r^{-1.5}$, the time that a satellite spends behind Ceres approximately follows $r^{0.5}$, i.e., increases with orbital radius. Within 15 Ceres radii, the maximum time that a satellite in circular orbit can spend behind Ceres is 2.7 h, while the full duration of our satellite search sequence is 9 h. Therefore, no satellite can be completely blocked by Ceres in our satellite search sequence.

For satellites with orbital radii greater than 15 Ceres radii, the search completeness drops sharply. This boundary is determined by the FOV of the Dawn FC. For satellites with orbital radii larger than the FOV, the probability for them to be in the FOV is proportional to r^{-1} for large r compared to Ceres radius, which approximately defines the shape of the completeness curve towards large r. At about 120 Ceres radii, the completeness drops to below 1%, which is considered the boundary of our satellite search. Note that the Hill radius of Ceres is 440 Ceres radii.

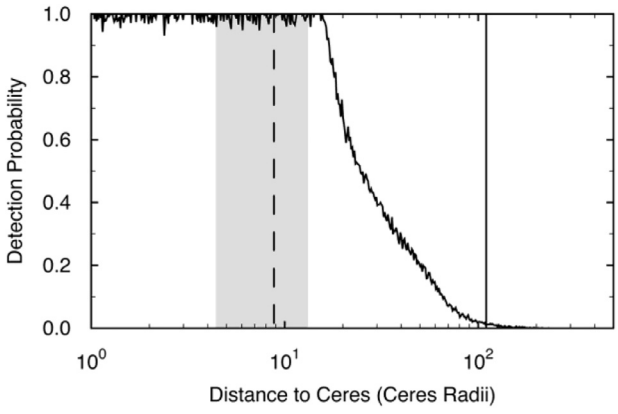

Fig. 9. Detection probability vs. orbital radius to Ceres using the FC field of view and pointing derived from a model of 10^6 satellites in orbit around Ceres. Shaded region is 1–3% of Hill radius (440 Ceres radii), dashed line is 0.02 of Hill radius and solid line is 0.25 Hill radius, regions where main-belt asteroid satellites have been found per Marchis et al. (2016).

As noted above, the completeness estimate from this simulation is entirely determined by the geometric parameters of our satellite search images, including the FOV, the image orientation, the orbital parameters of simulated satellites, and the timing of all the images. Therefore, the geometric completeness estimate is the same for a satellite of any size and is independent of the brightness detection limit that is constrained by detector sensitivity, sky background, scattered light from Ceres that is discussed in Section 4.3.

In considering the instrument response in a completeness analysis, a completeness curve as a function of distance to Ceres would be determined by the detector sensitivity, including detector noise, sky background, and scattered light from Ceres. This function would be called "brightness limited completeness" and is different for different size intervals of a possible Ceres' satellite. For example, if we consider a 10 km radius satellite, then its brightness limit completeness curve would be a straight line at 100% regardless of the distance from Ceres, because it is brighter than our detection limit anywhere in the image, even close to Ceres because it is much brighter than the scattered light. If we consider, e.g., a 1 km satellite, then its brightness completeness is low at close distance to Ceres because of the scattered light from Ceres, but becomes 100% at some distance where the Ceres scattered light is no longer an issue. If we consider a smaller satellite, say 100 m, then its completeness is probably 0 at close distance to Ceres where scattered light is overwhelming, but will only be probably 30% at large distance because its brightness is not much higher than sky background plus detector noise. The final completeness curve is the product of the geometric completeness curve and the brightness limit completeness curve for each size bin. Instead of calculated brightness completeness curves, Searcher 1 determined the upper limit for magnitude detection for each sequence searched and is discussed next.

4.3. Limiting magnitude and radius upper limits

The magnitude limit for each portion of the search depends on the effective exposure time determined from blinking of stacked images. For the purpose of this discussion, the limiting V-magnitude is that of the faintest detectable stars as determined by searcher 1. For OpNav 1 and OpNav 2, limiting magnitude was 10.8. For OpNavs 3–7, the ride-along image sets were stacked together in groups of 10 to give 18 images of 20 s exposure each. These were then blinked to look for brighter, faster objects, then restacked into 3 groups of 60 images to give 3 stacked frames of 120 s effective exposure time. Any moving objects in the 60 frame stacks brighter than V magnitude 12.8 would have been detected. These 120 s exposures are most sensitive to distant, slow moving satellites, those that would not move more than a pixel during the exposure.

The dedicated moon search images, with Ceres at the edge or outside of the field of view, consisted of 192 frames on one side of Ceres (Moon Search 1) and 256 off to the other (Moon Search 2) (Fig. 3). Given the approach geometry, these images allow for the possibility of an equatorial satellite between Dawn and Ceres to be observed in both image sets. Each set of 16 images was searched for fast moving objects. Then the stack of 16 was blinked against the other 3 stacked images to look for fainter objects. The 16 image stacks would have a limiting magnitude for moving object detection of about V = 11.7. If there was enough spatial overlap between hourly units then the entire 64 image set was stacked to give an effective exposure time of 128 s and these long exposures would be blinked for the deepest searches for distant satellites with a limit of about V = 12.8 magnitude. The final search was conducted during RC3. Any moving objects brighter than magnitude V = 10.5 would have been detected. None were found.

The limiting magnitudes were then corrected for illumination geometry using IAU HG (Dymock, 2007) photometric system with H = 3.17, G = 0.016 as derived from Dawn FC clear filter (F1, Sierks et al., 2011) approach data covering phase angles up to 155°. Then, using Ceres geometric albedo, 0.11 (Li et al., 2015), the upper limit to the size of any detectable satellite was calculated (Table 1). The possible radius of detectable satellites ranges from 191 to 113 m in OpNav 1 and 2. With the Ride Along imaging in OpNav 3–7, the detection limit is as small as 59 m (due to high phase angle) or 12 m at OpNav 7. The deepest dedicated satellite search processing resulted in a radius limit of 25 m. One of the RC3 searches also reached this same size limit while at a distance to Ceres of 14,000 km allowing the search to be conducted closer to Ceres than any previous search effort. Note that these results assume any satellite has the same geometric albedo as Ceres (0.11 for these calculations) and if the size limit is derived from the updated geometric albedo of 0.085 (Li et al., 2016) the limiting size would be 14% larger. These results extend the search for satellites of Ceres an order of magnitude below that reported by Bieryla et al. (2011) from Hubble Space Telescope and ground-based observations in 2003 and 2004, and a factor of two below the 2014 search with Hubble Space Telescope reported by DeMario et al. (2016). We also note that these size limits are 1–2 orders of magnitude smaller than the size of satellites found around other main belt asteroids, for example, Yang et al. (2016), Marsset et al. (2016), Descamps et al. (2011) and others noted below.

5. Discussion

Searches of processed framing camera images from the Dawn spacecraft have yielded no satellite of Ceres larger than 323 m or 12 m radius (the range of values at different observing sets listed in Table 1) and 16- or 5 m radius for Vesta (McFadden et al., 2015). To address the absence of satellites around the two largest and most massive asteroids and possibly constrain the conditions resulting in the existence or formation of natural satellites around other asteroids, we compiled the physical properties of 41 main belt asteroids with measured masses and diameter > 65 km (Baer, 2012), including those that have natural satellites (Johnston, 2015, 2016) (Table 2 and Fig. 10a–c). We also review and summarize efforts to place upper limits on the size of satellites with an eye to observing any relationship between the physical properties of asteroids *with* and those *without* satellites for purposes of revealing the conditions conducive to satellite formation associated with large asteroids.

5.1. Summary of previous satellite searches around protoplanets

A search for satellites around 2 Pallas, the third largest asteroid was conducted using adaptive optics on the Gemini Planet Imager and no moon was found to an observational limit of 0.25 km radius at < 1.2″ from Pallas (Marchis and Vega, 2014). Upper limits from null searches for 52 Europa (0.4 km radius, Gradie and Flynn, 1988), 15 Eunomia (0.2 km radius, Gradie and Flynn, 1988), and 324 Bamberga (0.2 km, Gradie and Flynn, 1988) have been reported. Millis et al. (1981) report no secondary occultations attributable to a companion for 3 Juno from 15 photometric observations. Twelve observed stellar occultations by 88 Thisbe (Millis et al., 1983) also produced no evidence of satellites. There are no reported satellite searches found in the literature for the 17 other asteroids listed in Table 2 with no satellites.

Of these forty-one, relatively large and massive main belt asteroids, 12 (~30%) do have satellites. One half of the 12 are multiple systems. 87 Silvia, has two moons (Marchis et al., 2005), as does 45 Eugenia (Merline et al., 1999, Marchis et al., 2007, 2008b), 93 Minerva (Marchis et al., 2005), 107 Camilla (Marsset et al., 2016; Storrs et al., 2001), 130 Elektra (Yang et al., 2014, 2016) and 216 Kleopatra (Marchis et al., 2008; Descamps et al., 2011). Five of these multiples have densities < 1.5 g/cm^3, and rotation periods less than 6 h, slightly faster than main belt asteroids in general, with rotation rates between 5–12 h (e.g. Pravec et al., 2002). 41 Daphne, and 121 Hermione (Descamps et al., 2009) each have a single satellite that is an order of magnitude or more, smaller than the primary. These satellite systems may have formed during reaccretion after a disruptive collision event (Marchis et al., 2005).

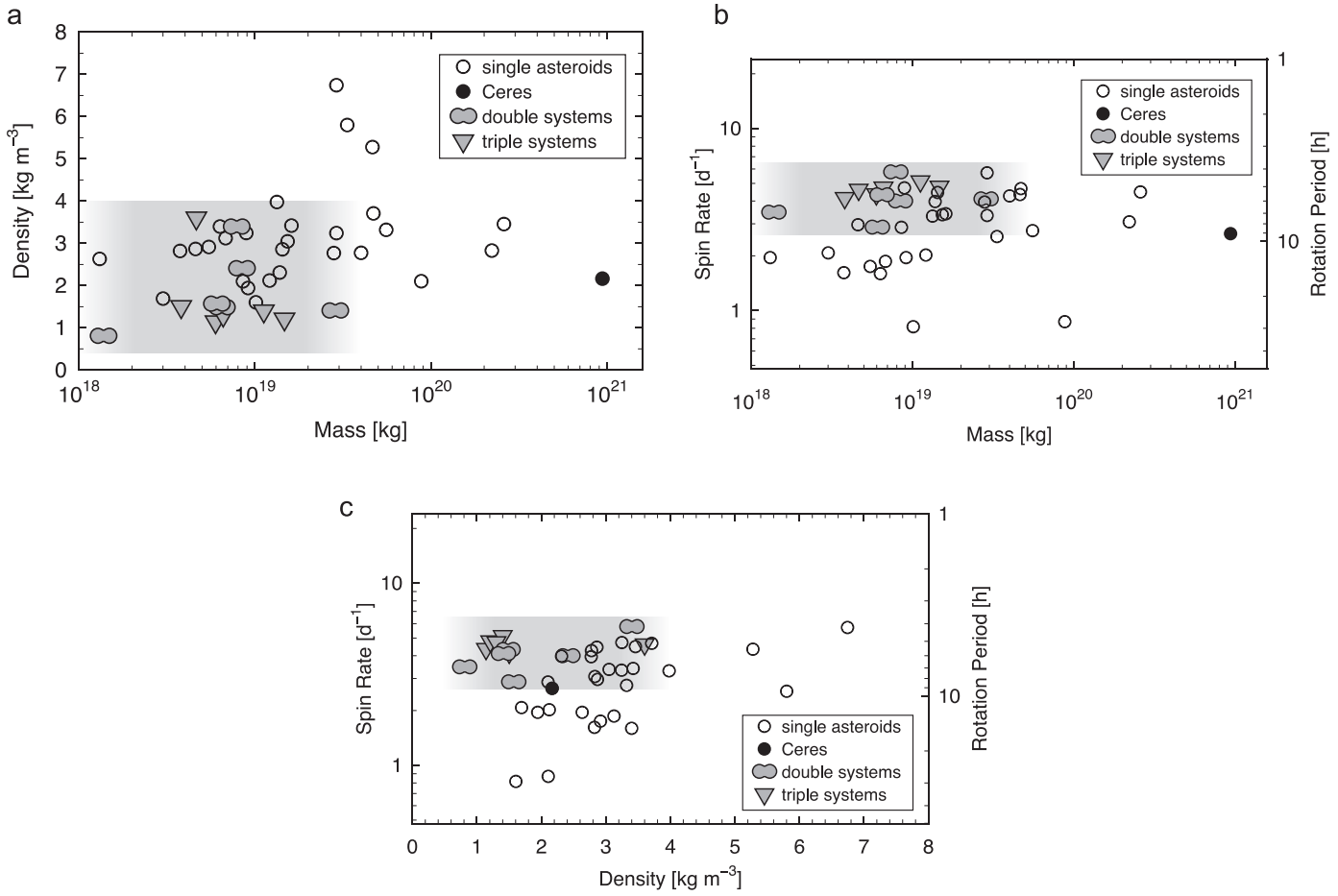

Fig. 10. (a) Density vs. Mass plot of asteroids without satellites (open circles) and those with satellites (grey lobed circles and inverted triangles). This plot implies no effect of local gravity on the presence of satellites. (b). Spin rate vs. mass for asteroids without (open circles) and with (lobed circles and inverted triangles) satellites. The spin rate of those with satellites varies across the shaded region and there is overlap between the two populations. Ceres is the filled circle. (c). Spin rate vs. Density of asteroids without satellites (open circles) and those with satellites (lobed circles and inverted triangles).

Their stability in time depends on resonances within the asteroid belt (e.g. Frouard and Compère, 2012).

5.2. Mass, density, spin rate of large asteroids

One would think that a massive, dense asteroid would favor retaining a co-orbiting satellite, however Fig. 10a indicates that the field of mass and density (shaded region) *with* satellites (filled lobes and inverted triangles) overlaps with asteroids that *don't* have satellites (open circles). Compare Ceres to the Pluto system that formed plausibly from a giant impact (Canup, 2005) and subsequent reaccretion after collision (Stern et al., 2006). Ceres' surface gravity is approximately half that of Pluto's (0.28/0.62) and 4 times greater (0.28/0.07) than that of asteroid 87 Sylvia, also a multiple system, as is Pluto. It seems that gravity is not the controlling factor for the existence of multiple asteroid systems. Neither mass nor density are indicators of the presence nor absence of a satellite suggesting that local gravity doesn't play a role in retention of material after catastrophic collision of an asteroid.

In Fig. 10b, spin rate is plotted against mass showing that the relatively massive asteroids with *no* satellites have a wider and overlapping range of rotation periods than those asteroids *with* satellites and that the spin distribution of asteroids with satellites ranges from 2.87–5.79 d^{-1}. On the other hand, Fig. 10c showing spin rate vs. density and Fig. 10a both show that most asteroids *with* satellites have lower density and therefore can be considered rubble piles. They generally have higher spin rates too. In Walsh and Jacobson (2015), they note that for large asteroids > 20 km (all in our sample are), YORP-related thermal effects are not significant and they are not likely to disrupt from this mechanism. This raises the question as to whether fast spinning asteroids disrupt or that disrupted asteroids are spun up as a consequence of disruption? In either case, high spin rate is a necessary but not sufficient condition that is associated with the presence of asteroid satellites. In the context of the data collated here, satellite formation mechanisms including post collision reaccretion and binary formation of asteroids, it seems that the larger asteroids that remain intact, are not likely to have natural satellites or exist as multiple systems.

5.3. Satellite formation mechanisms in context of large asteroids

Satellite formation mechanisms span a range of energies that most likely are triggered by collisions and probably depend on the internal structural properties of the primary body. High velocity impacts between objects of similar size are invoked to form Earth's (e.g. Canup and Asphaug, 2001) and Mars' moons (e.g. Craddock, 2011). Impacts on Vesta that likely produced the Veneneia and Rheasilvia impact basins (e.g. Schenk et al., 2012) were energetic enough to launch significant debris that formed the Vesta family (Asphaug, 1997) and sent fragments on collision course with Earth where they were found as basaltic achondrite

Table 2
Forty-one most massive asteroids and their physical parameters.

Number	Name	Mass (kg)	density (kg/m^3)	Radius (km)	Rot rate (h)	Spin rate (d^{-1})
1	Ceres	9.38E+20	2163	470.0	9.07	2.65
4	Vesta	2.59E+20	3456	261.0	5.35	4.49
2	Pallas	2.21E+20	2828	265.4	7.81	3.07
3	Juno	2.90E+19	3241	128.8	7.21	3.33
6	Hebe	1.33E+19	3978	93.1	7.27	3.30
7	Iris	1.53E+19	3047	106.3	7.14	3.36
8	Flora	6.80E+18	3123	80.5	12.87	1.87
9	Metis	8.91E+18	3245	86.9	5.08	4.73
10	Hygiea	8.79E+19	2104	215.3	27.62	0.87
11	Parthenope	5.46E+18	2913	76.5	13.72	1.75
13	Egeria	1.61E+19	3420	104.0	7.05	3.41
14	Irene	6.32E+18	3397	76.3	15.03	1.60
15	Eunomia	2.80E+19	2770	134.1	6.08	3.95
16	Psyche	2.90E+19	6743	132.0	4.20	5.72
17	Thetis	1.31E+18	2630	49.1	12.27	1.96
18	Melpomene	3.00E+18	1690	75.2	11.57	2.07
19	Fortuna	9.12E+18	1940	104.0	12.27	1.96
20	Massalia	4.59E+18	2867	72.6	8.10	2.96
22	Kalliope	7.87E+18	3400	84.2	4.15	5.79
24	Themis	8.53E+18	2100	99.0	8.37	2.87
29	Amphitrite	1.43E+19	2858	106.0	5.39	4.45
31	Euphrosyne	4.64E+19	5277	128.0	5.53	4.34
41	Daphne	8.43E+18	2410	94.2	5.99	4.01
45	Eugenia	5.97E+18	1140	107.6	5.70	4.21
48	Doris	1.21E+19	2120	110.9	11.89	2.02
52	Europa	4.00E+19	2774	151.0	5.63	4.26
87	Sylvia	1.47E+19	1205	142.9	5.18	4.63
88	Thisbe	1.38E+19	2310	112.6	6.04	3.97
93	Minerva	3.80E+18	1500	70.8	5.98	4.01
107	Camilla	1.12E+19	1400	129.4	4.84	4.95
121	Hermione	6.48E+18	1487	104.5	5.55	4.32
130	Elektra	6.60E+18	1300	182.0	5.23	4.59
216	Kleopatra	4.64E+18	3600	67.5	5.39	4.46
283	Emma	1.38E+18	810	148.0	6.90	3.48
324	Bamberga	1.01E+19	1602	114.5	29.43	0.82
511	Davida	4.70E+19	3708	144.7	5.13	4.68
532	Herculina	3.34E+19	5800	111.2	9.41	2.55
702	Alauda	6.06E+18	1570	97.4	8.35	2.87
704	Interamnia	5.55E+19	3319	159.4	8.73	2.75
762	Pulcova	2.86E+19	1410	68.5	5.84	4.11
804	Hispania	3.75E+18	2820	79.0	14.85	1.62

Notes: Masses from Baer (2012), densities from Carry (2012). Rotation and spin rates from wikipedia entries for each asteroid, referenced therein. Pink=no satellites, turquoise=binary, blue=tertiary system. See online version for interpretation of colors.

meteorites. Yet fragments did not remain in orbit as satellites (e.g. McFadden et al., 2015). Descamps and Marchis (2008) examine the physical and orbital characteristics of binary asteroids and suggest that asteroidal systems may result from rotational fission or mass shedding derived from an external torque. In Marchis et al. (2008b) the low density of some binary systems is noted. At the other end of the mass continuum and collision velocity scales, are recent models simulating collisions between small, low density, cometary nuclei (e.g. Jutzi and Asphaug, 2015) that in some circumstances produce bilobate shapes seen in some comet nuclei.

Ceres impacts were either not energetic enough to produce giant impact basins (not likely), or the volatile-rich nature of Ceres' interior (Thomas et al., 2005; McCord and Sotin, 2005; Castillo-Rogez and McCord, 2010; Rivkin et al., 2014) resulted in dissipation (sublimation with disintegration) of ejected debris. Another possibility is that local resonances produce short-lived orbits in the vicinity of Ceres. Winter et al. (2009), for example, show that local resonances can also preserve satellites orbiting asteroids, as in the case of 87 Silvia. With recent results from the Dawn mission (Park et al., 2016 and Marchi et al., 2016) our view of Ceres' interior includes its viscous nature and it is possible that energy transferred to Ceres upon impact may have been damped by Ceres' viscous interior, reducing the energy of ejected projectiles and thus increasing the rate of fall back onto Ceres surface. The volatile-rich nature of Ceres collisional debris is also mentioned in Rivkin et al. (2014) to explain the absence of a Ceres family of asteroids. We suggest a similar situation could explain the absence of satellites reported in this paper.

The aspects of satellite formation discussed here call for additional exploration of resonances associated with Ceres to further constrain both satellite formation and transport mechanisms from Ceres to Earth. The simplest answer for the case of Ceres is that the original composition of Ceres as rock and ice, along with the accretion process, formed a gravitationally relaxed asteroid that was not subsequently disrupted by impact-forming collisions. This state of Ceres has been proposed in Marchi et al. (2016) and found to be consistent with moment of inertia calculations by Park et al. (2016). Furthermore, the volatile-rich composition of bulk Ceres is also consistent with the absence of fragments from Ceres in the terrestrial meteorite collection. The absence of satellites in Ceres gravitational sphere of influence is therefore consistent with these independent results about Ceres from the Dawn mission (e.g. Russell et al., 2016 and references therein).

Instead of saying that satellites are missing, as we did in the case of Vesta (McFadden et al., 2015), it seems that the protoplanet formation process sweeps up debris and short-lived ejecta and that "proto-satellites" re-impact the surface. At Ceres and around other large, intact asteroids, nothing like what formed the Moon (Canup and Asphaug, 2001), nothing like what formed the satellites of the Giant planets and no catastrophic disruption that has been hypothesized to form multiple asteroids such as discussed in Walsh and Jacobson (2015), Frouard and Compère (2012) for the Sylvia system and Descamps et al. (2011), for the Kleopatra system, has occurred.

None of this is definitive, yet the fact remains that capture of satellites is unlikely. Ballistic trajectories of ejecta from impacts into elliptical orbits are also unlikely because a mechanism to change the orbit is lacking on a single body asteroid (Durda et al., 2004), and YORP is not a significant force for large bodies (Walsh and Jacobson, 2015). Catastrophic disruption, as modeled by Michel et al. (2001, 2004) is not applicable for the largest main belt asteroids, as their near-spherical shapes and high density (see Table 2) suggest that collisions were non-disruptive.

Do asteroids without satellites have an interior structure keeping them intact and unable to produce satellites orbiting their primary body today? Looking at their density (Table 2) compared with Earth's crustal density (2700 kg/m^3) as a reference for rock with strength, and considering what is known about the internal structure of some of these asteroids (Descamps and Marchis, 2008), it seems that asteroids with satellites are likely to be rubble piles, they have densities less than Earth's crust. Two exceptions are the M-type asteroids, 22 Kalliope (Descamps et al., 2008) and 216 Kleopatra (Descamps et al., 2011), both with density larger than that of Earth's crust. They have measured parameters supporting their metal-rich compositions, and are probably metal-rich rubble piles with density of 3,400 and 3,600 kg/m^3, respectively, considerably lower than ~7,000 kg/m^3 expected of a metal-dominated object. Both Kalliope and Kleopatra are arguably reaccreted asteroids from post-collisional disruption of metal-rich progenitors. Asteroids without satellites probably have internal structure and strength protecting them against complete disruption and subsequent satellite or binary formation.

6. Conclusions

We looked for satellites around Ceres using framing camera images on the Dawn spacecraft and found none larger than 12 m radius. Our search is complete down to a distance of ~15 Ceres radii or ~3% of the Hill radius, and we have searched to an upper limit of detection that is two orders of magnitude smaller than satellites found around other main belt asteroids. This search is also an order of magnitude smaller than previous attempts to find satellites of Ceres (DeMario et al., 2016).

In examining the physical properties of the 41 large and most massive asteroids, it seems that intact protoplanets do not have satellites and large asteroids *with* natural satellites are rubble piles, having low density and possibly spun up spin rates as a result of disruptive collisions that then reaccreted with one or more satellites. Large asteroids without satellites are: (1) not rubble piles, (2) have not experienced disruptive impacts, either because of dense interiors and/or relatively low energy impacts, and (3) are located in a region of the asteroid belt with local resonances that are unstable to multiple systems. Such large bodies without satellites can be considered intact protoplanets, some of which are known to be differentiated. These results are consistent with results of the Dawn mission derived from its instrument complement (e.g. Russell et al., 2012; Russell et al., 2016 and references therein).

Acknowledgements

The satellite working group would like to thank the Dawn project for their support of this effort. We thank the flight team for their participation, trajectory design and successful flight operations. This work is supported through NASA's Discovery Program. Part of this work was carried out at the Jet Propulsion Laboratory, California Institute of Technology, and Planetary Science Institute under a contract with NASA to UCLA, NASA contract number, NNM05AA86C. The Framing Camera project is financially supported by the Max Planck Society Germany and the German Aerospace Agency, DLR.

Supplementary materials

Supplementary material associated with this article can be found, in the online version, at doi:10.1016/j.icarus.2018.02.017.

References

Acton, C.H., 1996. Ancillary data services of NASA's navigation and ancillary information facility. Planet. Space Sci. 44 (1), 65–70.
Asphaug, E., 1997. Impact origin of the Vesta family. Meteorit. Planet. Sci. doi:10.1111/j.1945-5100.1997.tb01584.x.
Baer, J., 2012. Planetary Data System file: EAR-A-COMPIL-5-ASTMASS-V3.0.
Bastian, U., Roser, S., 1993. Catalog of Positions and Proper Motions: South. Astron. Rechen Inst., Heidelberg.
Bessell, M.S., 1990. UBVRI passbands. Publ. Astron. Soc. Pac. 102, 1181–1199. http://iopscience.iop.org/article/10.1086/132749/meta.
Bieryla, A., et al., 2011. Astron. J. 141, 197. doi:10.1088/0004-6256/141/6/197.
Busch, M.W., Kulkarni, S.R., Conrad, A., 2009. No satellites detected around 21 Lutetia. Icarus. http://dx.doi.org/10.1016/j.icarus.2009.06.025.
Canup, R.M., Asphaug, E., 2001. Origin of the Moon in a giant impact near the end of Earth's formation. Nature 412, 708–712. doi:10.1038/35089010, (16 August 2001).
Canup, R.M., 2005. A Giant impact origin of Pluto-Charon. Science 307 (5709), 546–550. doi:10.1126/science.1106818, 28 January.
Carry, B., 2012. Density of Asteroids. Planet. Space Sci. 73, 98–118. http://dx.doi.org/10.1016/j.pss.2012.03.009.
Castillo-Rogez, J.C., McCord, T.B., 2010. Ceres' evolution and present state constrained by shape data. Icarus 205, 443–459. http://dx.doi.org/10.1016/j.icarus.2009.04.008.
Chapman, C.R., et al., 1995. Discovery and physical properties of Dactyl, a satellite of asteroid 243 Ida. Nature 374, 783–785. doi:10.1038/374783a0.
Craddock, R.A. Are Phobos and Deimos the result of a giant impact? http://dx.doi.org/10.1016/j.icarus.2010.10.023.
DeMario, B.E., Schmidt, B.E., Mutchler, M.J., Li, J.-Y., McFadden, L.A., McLean, B.J., Russell, C.T. Results of a Hubble Space Telescope Search for Natural Satellites of Dwarf Planet 1 Ceres http://dx.doi.org/10.1016/j.icarus.2016.07.005.
Descamps, P., Marchis, F., 2008. Angular momentum of binary asteroids: Implications for their possible origin. Icarus 193, 74–84. https://doi.org/10.1016/j.icarus.2007.07.024.
Descamps, P., et al., 2008. New determination of the size and bulk density of the binary asteroid 22 Kalliope from observations of mutual eclipses. Icarus 196 (2), 578–600. doi:10.1016/j.icarus.2008.03.014.
Descamps, P., et al., 2009. New insights on the binary asteroid 121 Hermione. Icarus 203, 88–101. doi:10.1016/j.icarus.2009.04.032.
Descamps, P., et al., 2011. Triplicity and physical characteristics of Asteroid (216) Kleopatra. Icarus. http://dx.doi.org/10.1016/j.icarus.2010.11.016.

Durda, D.D., Bottke, W.F., Enke, B.L., Merline, W.J., 2004. The formation of asteroid satellites in large impacts: results from numerical simulations. Icarus 167, 382–396. doi:10.1016/j.icarus.2003.09.017.
Dymock, R., 2007. The H and G magnitude system for asteroids. J. British Astron. Assoc. 117, 342–343.
Frouard, J., Compère, A., 2012. Instability zones for satellites of asteroids: the example of the (87) Sylvia system. Icarus, http://dx.doi.org/10.1016/j.icarus.2012.04.026.
Gehrels, T., Drummond, J.D., Levenson, N.A., 1987. The absence of satellites of asteroids. Icarus 70, 257–263. doi:10.1016/0019-1035(87)90133-3.
Gradie, J., Flynn, L., 1988. A search for satellites and dust belts around asteroids: Negative results. Lunar Planet. Sci. XIX. Abstract 405. 1988LPI....19..405G.
Johnston, W.R., 2015. Binary minor Planets V8.0. EAR-A-COMPIL-5-BINMP-V8.0. NASA Planet. Data Syst.
Johnston, W.R. Asteroids with Satellites http://www.johnstonsarchive.net/astro/asteroidmoons.html, last updated 22 October 2016. Accessed Nov. 18.
Jutzi, M., Asphaug, E., 2015. The shape and structure of cometary nuclei as a result of low-velocity accretion. Science. http://dx.doi.org/10.1126/science.aaa4747.
Krebs, J.P., Pissavin, P., Vilaire, D., 2000. SED 16 autonomous star tracker. Spacecraft Guidance Navig. Control Syst. 425.
Lang, et al., 2010. Astrometry.net: blind astrometric calibration of arbitrary astronomical images. Astron. J. 137, 1782–1800.
Lasker, B., et al., 2008. The second generation guide star catalog: description and properties. Astron. J. 136 (2008), 735–766.
Li, J.-Y., Crep, J., Serabyn, G., McFadden, L, Williams, J., Crow, C., 2010. Search for satellites around asteroids with coronagraphic high-contrast imaging on adaptive optics. American Astronomical Society, DPS meeting #42, #39.30. Bull. Am. Astron. Soc. 42, 1038.
Li, et al., 2015. The Phase function of Ceres at high phase angles. In: 46th Lunar and Planetary Conference, held March 16-20, 2015 at The Woodlands, p. 2565. TX LPI Contribution No. 1832 http://www.hou.usra.edu/meetings/lpsc2015/pdf/2565.pdf.
Li, et al., 2016. Spectrophotometric modeling and mapping of Ceres. EGU General Assembly 2016, held 17-22 April 2016 2016EGUGA..1817302L.
Marchi, S. et al. 2016. The missing large impact craters on Ceres. doi:10.1038/ncomms12257.
Marchis, F., Descamps, P., Hestroffer, D., Bertheir, J, 2005. Discovery of the triple asteroidal system 87 Sylvia. Nature doi:10.1038/nature04018.
Marchis, F., et al. 2007, S/2004 (45) 1. IAUC 8817.
Marchis, F., et al. 2008, S/2008 (216) 1 and S/2008 (216) 2. IAUC 8980.
Marchis et al. 2008b, Main Belt binary asteroidal systems with circular mutual orbits. https://doi.org/10.1016/j.icarus.2008.03.007.
Marchis, F., et al. 2009. S/2009 (93) 1 and S/2009 (93) 2. IAUC 9069.
Marchis, F., Vega, D., 2014. The potential of extreme adaptive optics systems for Asteroid studies. American Geophysical Union, Fall Meeting 2014 abstract #P43F-08.
Margot, J.-L., et al., 2002. Binary Asteroids in the Near-Earth object population. Science doi:10.1126/science.1072094.
Margot, J.-L., et al., 2015. Asteroid systems: binaries, triples, and pairs. In: Michel, P., et al. (Eds.), Asteroids IV. U. Arizona Press, pp. 355–374.
Marsset M. et al. 2016. S/2016 (107) 1. IAUC 9282.
Maxim-DL-IP, 2008 Maxim DL Version 5 http://www.cyanogen.com/.
McCord, T.B., Sotin, C., 2005. J. Geophys. Res.
McFadden, L.A., et al., 2012. Upper limits on the size of satellites of Asteroid (4) Vesta from 2007 Hubble Space Telescope observations. Icarus 220 (2012), 305–310. http://dx.doi.org/10.1016/j.icarus.2012.05.002.
McFadden, L.A., et al., 2015. Vesta's missing moons: comprehensive search for natural satellites of Vesta by the Dawn spacecraft. Icarus. http://dx.doi.org/10.1016/j.icarus.2015.04.038.
Merline, W.J., et al., 1999. Discovery of a moon orbiting the asteroid 45 Eugenia. Nature doi:10.1038/44089.
Merline, et al., 2001. An automated search for moons during approach of the NEAR spacecraft to asteroid Eros. In: Proc. 6th International Symposium on Artificial Intelligence, Robotics and Automation in Space 2001 (Montreal), Paper #AM128.
Merline, W.J., Weidenschilling, S.J., Durda, D.D., 2002. In: Bottke, Cellino, Paolicchi, Binzel (Eds.), Asteroids Do have satellites. Asteroids III. U. Arizona Press, Tucson AZ, pp. 289–312.
Michel, P., Benz, W., Tanga, P., Richardson, D.C., 2001. Collisions and gravitational *Reaccumulation: forming Asteroid Families and Satellites*. Science 294 (5547), 1696–1700. doi:10.1126/science.1065189, 23 Nov 2001.
Michel, P., Benz, W., Richardson, D.C., 2004. Catastrophic disruption of asteroids and family formation: a review of numerical simulations including both fragmentation and gravitational reaccumulations. Planet. Space Sci. 52, 1109–1117.
Millis R.L., et al. (1981) The diameter of Juno from its occultation of AG+0 deg 1022. doi:10.1086/112889.
Millis, R.L., Wasserman, L.H., Franz, O.G., White, N.M., Bowell, E., Klemola, A., 1983. The diameter of 88 THISBE from its occultation of SAO 187124. Astron. J. 88, 229–235 Feb. 1983.
Nathues, A., Sierks, H., Gutierrez-Marques, P., Ripken, J., Hall, I., Buettner, I., Schaefer, M., Chistensen, U., 2016a. Dawn FC2 Calibrated Ceres Images V1.0, OpNav 1. DAWN-A-FC2-3-RDR-CERES-IMAGES-V1.0:0032651 to 0032690, NASA Planetary Data System, 2016.
Nathues, A., Sierks, H., Gutierrez-Marques, P., Ripken, J., Hall, I., Buettner, I., Schaefer, M., Chistensen, U., 2016b. Dawn FC2 Calibrated Ceres Images V1.0, OpNav 2. DAWN-A-FC2-3-RDR-CERES-IMAGES-V1.0:0032691 to 0032730, NASA Planetary Data System, 2016.
Nathues, A., Sierks, H., Gutierrez-Marques, P., Ripken, J., Hall, I., Buettner, I., Schaefer, M., Chistensen, U., 2016c. Dawn FC2 Calibrated Ceres Images V1.0, Moon Search 1a. DAWN-A-FC2-3-RDR-CERES-IMAGES-V1.0:0032731 to 0032922, NASA Planetary Data System, 2016.
Nathues, A., Sierks, H., Gutierrez-Marques, P., Ripken, J., Hall, I., Buettner, I., Schaefer, M., Chistensen, U., 2016d Dawn FC2 Calibrated Ceres Images V1.0, OpNav 3. DAWN-A-FC2-3-RDR-CERES-IMAGES-V1.0:0032923 to 0033142, NASA Planetary Data System, 2016.
Nathues, A., Sierks, H., Gutierrez-Marques, P., Ripken, J., Hall, I., Buettner, I., Schaefer, M., Chistensen, U., 2016e. Dawn FC2 Calibrated Ceres Images V1.0, Moon Search 1b. DAWN-A-FC2-3-RDR-CERES-IMAGES-V1.0:0033143 to 0033398, NASA Planetary Data System, 2016.
Nathues, A., Sierks, H., Gutierrez-Marques, P., Ripken, J., Hall, I., Buettner, I., Schaefer, M., Chistensen, U., 2016f. Dawn FC2 Calibrated Ceres Images V1.0, OpNav 4. DAWN-A-FC2-3-RDR-CERES-IMAGES-V1.0:033829 to 0034048, NASA Planetary Data System, 2016.
Nathues, A., Sierks, H., Gutierrez-Marques, P., Ripken, J., Hall, I., Buettner, I., Schaefer, M., Chistensen, U., 2016g. Dawn FC2 Calibrated Ceres Images V1.0, OpNav 5. DAWN-A-FC2-3-RDR-CERES-IMAGES-V1.0:0034049 to 0034268, NASA Planetary Data System, 2016.
Nathues, A., Sierks, H., Gutierrez-Marques, P., Ripken, J., Hall, I., Buettner, I., Schaefer, M., Chistensen, U., 2016h. Dawn FC2 Calibrated Ceres Images V1.0, OpNav 6. DAWN-A-FC2-3-RDR-CERES-IMAGES-V1.0:0034269 to 0034488, NASA Planetary Data System, 2016.
Nathues, A., Sierks, H., Gutierrez-Marques, P., Ripken, J., Hall, I., Buettner, I., Schaefer, M., Chistensen, U., 2016i. Dawn FC2 Calibrated Ceres Images V1.0, OpNav 7. DAWN-A-FC2-3-RDR-CERES-IMAGES-V1.0:0034489 to 0034708, NASA Planetary Data System, 2016.
Nathues, A., Sierks, H., Gutierrez-Marques, P., Ripken, J., Hall, I., Buettner, I., Schaefer, M., Chistensen, U., 2016j. Dawn FC2 Calibrated Ceres Images V1.0, RC3 High Phase North 1. DAWN-A-FC2-3-RDR-CERES-IMAGES-V1.0:035432 to 0035971, NASA Planetary Data System, 2016.
Noll, K., Grundy, W.M., Stephens, D.C., Levison, H.F., Kern, S.D., 2008. Evidence for two populations of classical transneptunian objects: The strong inclination dependence of classical binaries. Icarus doi:10.1016/j.icarus.2007.10.022.
Park, R.S., et al., 2016. A partially differentiated interior for (1) Ceres deduced from its gravity field and shape. Nature doi:10.1038/nature18955.
Polanskey, C.A., Joy, S.P., Raymond, C.A., Rayman, M.D., 2014. Architecting the Dawn Ceres Science Plan. SpaceOps Conferences, 5-9 May 2014, Pasadena, CA, 13th International Conference on Space Operations 2014 doi:10.2514/6.2014-1720.
Polanskey, C.A., Joy, S.P., Raymond, C.A., Rayman, M.D., 2016. Dawn Ceres Mission: science operations performance. In: Proceedings of SpaceOps 2016.
Pravec, P., Harris, A.W., Michalowski, T., 2002. In: Bottke, W.F. (Ed.), Asteroid Rotations, in Asteroids III. U of Arizona Press, pp. 113–122.
Raab, H, 2013. Astrometrica Accessed November 7. http://www.astrometrica.at.
Rayman, M.D., Mase, R.A., 2014. Dawn's exploration of Vesta. Acta Astron. 94, 159–167. doi:10.1016/j.actaastro.2013.08.003.
Rayman, M.D., 2017. Dawn at Ceres: the first exploration of the first Dwarf planet. 68th International Astronautical Congress, 25-29 September 2017, Adelaide, Australia, Paper IAC-17.A3.4A.2x39024.
Rivkin, A.S., Asphaug, E., Bottke, W.F., 2014. The case of the missing Ceres family. Icarus 243, 429–439. doi:10.1016/j.icarus.2014.08.007.
Russell, C.T., et al., 2012. Dawn at Vesta: testing the Protoplanetary paradigm. Science 336. doi:10.1126/science.1219381.
Russell, C.T., et al., 2016. Dawn arrives at Ceres: exploration of a small, volatile-rich world. Science 353. http://science.sciencemag.org/content/353/6303/1008.
Ryan, W.H., et al., 2004. 3782 Celle: discovery of a binary system within the Vesta family of asteroids. Icarus. http://dx.doi.org/10.1016/j.pss.2004.07.006.
Samus, N.N., Kazarovets, E.V., Durlevich, O.V., 2001. General catalogue of variable stars. Odessa Astron. Publ. 14 (2001), 266.
Schröder, S.E., et al. 2013. In-flight calibration of the Dawn Framing Camera, doi:10.1016/j.icarus.2013.07.036.
Schenk, P., et al. 2012. The geologically recent giant impact basins at Vesta's South Pole. doi:10.1126/science.1223272.
Sierks, H., et al., 2011. The Dawn framing camera. Space Sci. Rev. 163, 263–327. http://dx.doi.org/10.1007/s11214-011-9745-4.
Stern, S.A., Weaver, H.A., Steffl, A.J., Mutchler, M.J., Merline, W.J., Buie, M.W., Young, E.F., Young, L.A., Spencer, J.R., 2006. A giant impact origin for Pluto's small moons and satellite multiplicity in the Kuiper belt. Nature 439, 946–948. doi:10.1038/nature04548.
Stetson, P.B., 1987. DAOPhot-A computer program for crowded-field stellar photometry Publ. Astron. Soc. Pac. 99 (1987), 191–222. http://dx.doi.org/10.1086/131977.
Storrs, A., Vilas, F., Landis, R., Wells, E., Woods C., Zellner, B and Gaffey, M. 2001. S/2001 (107) 1. IAU Circular No. 7599.
Thomas, P.C. Nature, volume 437, pages 224–226 (08 September 2005). doi:10.1038/nature03938.
Vanelli, C.Anthony, Swenka, Edward, Smith, Brett, 2008. Verification of pointing constraints for the Dawn Spacecraft. AIAA/ASS Astrodynamics Specialist Conference.
Veverka, J., et al., 1999. NEAR encounter with Asteroid 253 Mathilde: overview. Icarus 140, 3–16 Article ID icar.1999.6120.
Walsh, K.J., Jacobson, S.A., 2015. In: Michel, P., DeMeo, F., Bottke, W.F. (Eds.), Formation and Evolution of Binary Asteroids, Asteroids IV. U. Arizona Press, Tucson, AZ, pp. 375–393.

Walsh, K.J., 2009. Asteroids with satellites: inventory, properties, and prospects for future discoveries. Earth Moon Planet 105, 193–199. doi:10.1007/s11038-009-9302-2.
Winter, O.C., et al., 2009. On the stability of the satellites of asteroid 87 Sylvia. MNRAS 395, 218–227. https://doi.org/10.1111/j.1365-2966.2009.14564.x.
Yang, B, et al. S/2014 (130) 1. CBET 4036. http://www.cbat.eps.harvard.edu/cbet/004000/CBET004036.txt.
Yang, B., et al. 2016. doi:10.3847/2041-8205/820/2/L35.
Zacharias, et al., 2010. The third US Naval observatory CCD astrograph catalog (UCAC3). Astron. J. 139 (2010), 2184–2199.